Broadband multifunctional plasmonic polarization converter based on multimode interference coupler

Optik - International Journal for Light and Electron Optics 286 (2023) 170978

Contents lists available at ScienceDirect

Optik - International Journal for Light and Electron Optics

journal homepage: www.elsevier.com/locate/ijleo

Original research article

Broadband multifunctional plasmonic polarization converter based on multimode interference coupler

Hamed Pezeshki [a,b,c,*], Bert Koopmans [a,b], Jos J.G.M. van der Tol [b]

[a] Department of Applied Physics and Science Education, Eindhoven University of Technology, Eindhoven, 5612 AZ, Netherlands
[b] Eindhoven Hendrik Casimir Institute, Center for Photonic Integration, Eindhoven University of Technology, Eindhoven, 5600 MB, Netherlands
[c] EFFECT Photonics B.V., Eindhoven, 5616 LZ, Netherlands

ARTICLE INFO

Keywords:
Plasmonics
Polarization converter
Half-wave plate
Quarter-wave plate
Photonic integrated circuit
Indium phosphide

ABSTRACT

We propose a multifunctional integrated plasmonic–photonic polarization converter for polarization demultiplexing in an indium-phosphide membrane on silicon platform. By using a compact 1 × 4 multimode interference coupler, this device can provide simultaneous half-wave plate (HWP) and quarter-wave plate (QWP) functionalities. Our device employs a two-section HWP to obtain a very large conversion efficiency of ≥ 91% over the entire C to U telecom bands, while it offers a conversion efficiency of ≥ 95% over ~ 86% of the C to U bands. Our device also illustrates QWP functionality, where the transmission contrast between the transverse electric and transverse magnetic modes is ≈ 0 dB over the whole C band and 55% of the C to U bands. Using this functionality, our device generates two quasi-circular polarized beams with opposite spins and topological charges of $l = \pm 1$, based on only one input polarization, and one incoming light beam direction. We expect that this device can be a promising building block for the realization of ultracompact on-chip polarization demultiplexing and lab-on-a-chip biosensing platforms. Finally, our proposed device allows the use of the polarization and angular momentum degrees of freedom, which makes it attractive for quantum information processing.

1. Introduction

Indium phosphide (InP) membrane on silicon (IMOS) is a promising platform for the fabrication of low cost and large scale passive and active photonic integrated circuits (PICs), e.g. for applications in telecom [1,2], due to its compatibility with complementary metal oxide semiconductor (CMOS) processes. The high refractive index difference ($\Delta n \approx 2$) between its core and cladding enables large scale integration of photonic devices [3,4] and photonics–electronics convergence on a single chip [5]. However, the large refractive index difference makes it harder to obtain polarization independence in photonic devices [6]. Meanwhile, control over the polarization in PICs for polarization-independent operations of chips and for functions like polarization (de)multiplexing and polarization switching, is of great importance [7–9]. Hence, the development of an integrated polarization converter (PC) with a small footprint to support polarization diversity, as well as to convert the polarization state of light in PICs at will, has attracted a lot of attention during recent decades.

So far, several design proposals have been made, based on either mode evolution or mode interference. The PCs based on mode evolution implement adiabatic mode conversion between the two polarization states of a waveguide mode [10–14], and are typically long (≥ 100 μm). In contrast, shorter PCs use the interference between two orthogonal beating modes, propagating through a symmetry-broken waveguide [15–17]. The majority of the proposed PCs based on mode interference were developed with slanted

* Corresponding author at: Department of Applied Physics and Science Education, Eindhoven University of Technology, Eindhoven, 5612 AZ, Netherlands.
E-mail addresses: h.pezeshki@tue.nl, hamedpezeshki@effectphotonics.com (H. Pezeshki).

https://doi.org/10.1016/j.ijleo.2023.170978
Received 9 November 2022; Received in revised form 27 April 2023; Accepted 17 May 2023
Available online 26 May 2023

waveguides [18–20] and narrow trenches [21–23]. However, such approaches entail either a large footprint or a complex fabrication process [24].

It has been demonstrated that a plasmonic metal layer can overcome the above-mentioned challenges by enhancing the birefringence between the two beating modes using surface plasmon polaritons (SPPs), as well as offering a simple fabrication process. Early works on designs of integrated half-wave plates (HWPs) based on metal layers, show that large ohmic losses [16], caused by SPPs, can be decreased by placing a low-refractive index thin spacer layer at the metal–dielectric interface [17,25]. Komatsu et al. [25] and Caspers et al. [17] presented HWPs with insertion losses (ILs) of ∼5 and > 2 dB for device lengths of 11 and 5 μm, respectively. Later on, other groups reported SPP-based HWPs with a high polarization conversion efficiency (PCE) of 97% with an IL of ∼2 dB. Despite works done so far, broadband and multifunctional operation has not been addressed sufficiently yet.

There have also been some reports on the integrated quarter-wave plates (QWPs) using a plasmonic metal layer. Gao et al. [26] theoretically presented an integrated hybrid QWP based on plasmonics at λ_0=1.55 μm, where the PC's length was 1.5 μm. Liang et al. [27] theoretically showed a QWP with one-way angular momentum conversion at λ_0=1.55 μm, by placing a L-shaped metal layer with a length of 2.8 μm on a square photonic waveguide with a minimum birefringence, which is attached to a 2.4 μm long rectangular photonic waveguide with high birefringence. However, as shown in this paper, a better strategy would be to place the metal layer on a rectangular birefringence waveguide to further boost the birefringence for a shorter length of the metal layer. This, in turn, results in lower absorption loss (i.e. heat dissipation) by the metal layer, which is crucial for the performance efficiency of devices on a photonic chip. Moreover, there have been some reports on the design of an integrated QWP based on aluminum gallium arsenide (AlGaAs) [28] as well as with graphene in the Terahertz regime [29] by launching linearly polarized light at 45°. Both designs have very long converter sections of ∼53 μm and 145 μm, respectively. However, in the latter case, they achieved active adjustment of the polarization state of light through variation of the graphene's Fermi level. Despite several works done so far on both integrated HWP and QWP, design of a broadband multifunctional PC, to provide both polarization and angular momentum degrees of freedom, has not been investigated. A multifunctional device allows standardization, and thus cost reductions, while still supporting a wide range of applications [30].

In this paper, we introduce a multifunctional PC through the use of a compact and efficient 1 × 4 multimode interference coupler (MMI) with an ultrabroad operational wavelength range. Our proposed device presents a HWP functionality based on a two-section PC design to achieve optimum conversion efficiency and to improve fabrication tolerance. Note that the explanation of this approach is beyond the scope of this paper and interested readers are referred to our previous work by Van der Tol et al. [31]. According to results obtained with a three dimensional finite-difference time-domain (FDTD) method, Lumerical-FDTD in conjunction with its built-in parameter sweep utility [32], the HWP functionality of our proposed device offers a PCE of ≥ 91% over the C to U telecom bands, while PCE is ≥ 95% over ∼ 86% of this wavelength range. This implies that the HWP functionality possesses a polarization extinction ratio (PER) of better than 13 dB in the above-mentioned range, with a maximum of 38.4 dB at λ_0= 1.563 μm.

By taking advantage of the mirror symmetry in a MMI, we propose a device with a QWP functionality, by which two quasi-circular polarized beams with opposite spins (due to the transverse spin angular momentum, SAM) are generated using only one input polarization, and one incoming light beam direction. Our QWPs function efficiently, offering a transmission contrast of ≈ 0 dB between the transverse electric and transverse magnetic (TE_0 and TM_0) modes over the wavelength range of λ_0=1.53 to 1.61 μm, covering the whole C band and moreover 55% of the C to U telecom bands. The longitudinal electric field component of the generated quasi-circular polarized beams carry longitudinal orbital angular momentum (OAM) [33,34] with topological charges of $l = \pm 1$. Having two quasi-circular polarized beams simultaneously on a chip can be potentially attractive not only for on-chip telecom applications such as mode/polarization-(de)multiplexing [35], on-chip magneto-plasmonics [36,37], as well as quantum information processing [38], but also for biosensing applications including circular dichroism spectroscopy [39] and nanoparticle movement [40] using a longitudinal OAM.

2. Design structure and considerations

We propose a device based on the IMOS platform to provide different polarizations: linear TE_0 and TM_0 modes, as well as two quasi-circular polarized beams with opposite spins. It is composed of a 1 × 4 MMI for dividing a TE_0-polarized light into four output waveguides, as well as a PC section for performing HWP and QWP functionalities (see Fig. 1). The output waveguide 1 (O1) is connected to a rectangular waveguide and outputs a TE_0 mode. To obtain the quasi-circular polarized beams with opposite spins, we designed two plasmonic QWPs on top of the O2 and O3 waveguides, which are mirrored relative to each other. These created states will exist over propagation lengths that are much smaller than the TE_0-TM_0 beat length of ∼ 77.5 μm for a $\Delta n_{TE_0\text{-}TM_0} \sim 0.02$. The advantage of our approach over the previous approaches is that we illustrate QWPs with opposite spins using one device, without reversing the direction of light propagation. This makes it attractive for applications that require both spins simultaneously on a single chip. Finally, to obtain a TM_0 mode, we designed a plasmonic HWP, as a top cladding on the O4 waveguide. The proposed HWP is a two-section PC which consists of a combination of a QWP and a three quarter-wave plate (TQWP). We chose this approach to achieve our objectives of highly efficient conversion efficiency over an ultrabroad wavelength range, as well as enhanced fabrication tolerance, as demonstrated in [31]. Using this approach, the length of the converter is two times that of a single-section HWP.

The MMI section has a length and a width of l_{MMI} = 36 μm and w_{MMI} = 9 μm, respectively. In order to have an ultralow loss 1 × 4 MMI, we provide the coupling between the MMI section and the input as well as the output waveguides using linear tapers with a length and a width of l_{taper} = 8 μm and w_{taper} = 2 μm, respectively, creating smooth mode transitions between the input,

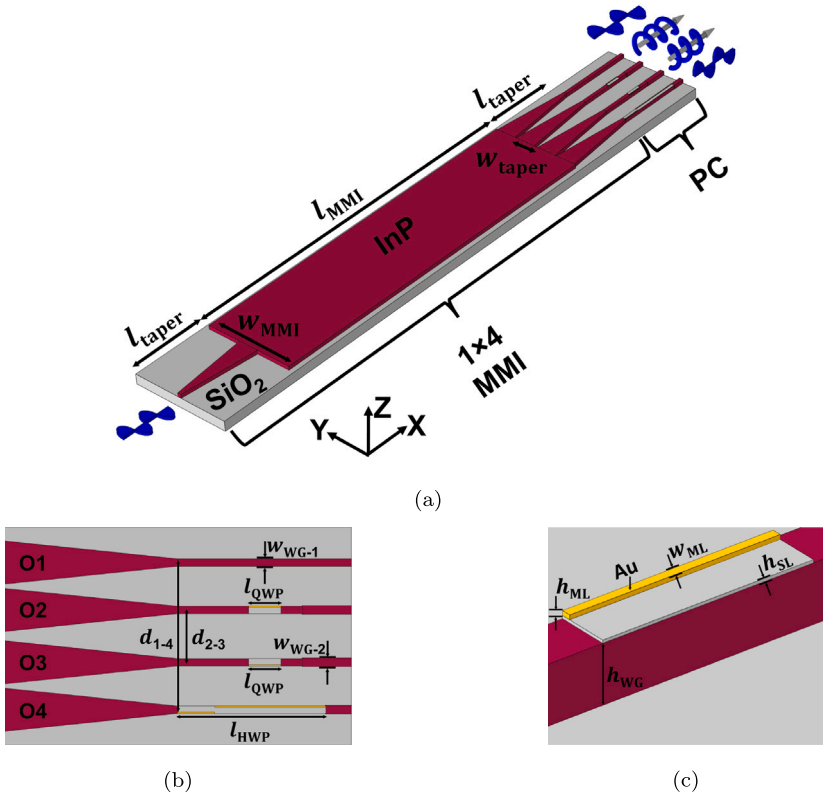

Fig. 1. Schematic of the proposed multifunctional polarization converter (PC). (a) Perspective view that shows the device is composed of a 1 × 4 multimode interference coupler (MMI) and a PC section. The lengths and widths of the MMI and tapers are indicated with l_{MMI}, l_{taper}, w_{MMI}, and w_{taper}, respectively. (b) Top view of the PC section showing the distances between the output waveguides O1(2) and O4(3) by d_{1-4} and d_{2-3}, respectively. The widths of the waveguide sections are presented by w_{WG-1} and w_{WG-2} and the lengths of the quarter-wave plates (QWPs) and half-wave plate (HWP) are shown by l_{QWP} and l_{HWP}, respectively. (c) Perspective view of a PC in which w_{ML} and h_{ML} are the width and height of the metal layer of the PC, h_{SL} and h_{WG} are the heights of the spacer layer and waveguide, respectively.

MMI, and output sections. Fig. 1(b) shows the top view of the PC section in which the center-to-center distances between the O1(2) and O4(3) waveguides are d_{1-4} = 6.75 and d_{2-3} = 2.4 μm, respectively. The QWPs devices on the O2 and O3 waveguides have a plasmonic cladding with a length of l_{QWP} = 1.48 μm to transform a TE_0 mode into quasi-circular polarized beams with two opposite spins. The designed HWP, with a total length of l_{HWP} = 6.8 μm, is designed as a top cladding on the O4 waveguide to transform a TE_0 mode to a TM_0 mode. The input and O1 waveguides have a width of w_{WG-1} = 0.34 μm, while the O2 to O4 waveguides are linked with waveguides with a different width of w_{WG-2} = 0.4 μm to minimize the birefringence in end parts of the waveguides, i.e. $\Delta n_{TE_0\text{-}TM_0} \sim 0.02$. The height of all photonic components are equal to h_{WG} = 0.39 μm. The width and height of all the plasmonic metal layers, as well as the height of silica (SiO_2) spacer layer are the same in the O2 to O4 waveguides, i.e. w_{ML} = 0.03 μm, h_{ML} = 0.03 μm, and h_{SL} = 0.02 μm, respectively (see Fig. 1(c)). All geometrical parameters of the device are listed in Table 1. As indicated in Fig. 1, the materials for the waveguides and MMI, substrate and the spacer layer beneath the plasmonic components are InP and SiO_2, whose parameters come from [41], and the material for the plasmonic components is gold (Au) [42].

The performance of the MMI is examined in Section 3.1 by calculating the transmission of its output waveguides and insertion loss (IL_{MMI} in dB). The insertion loss is obtained as the ratio of the superposition of all output powers to the input power:

$$IL_{MMI} = -10 \times \log((P^{O1} + P^{O2} + P^{O3} + P^{O4})/P^{In}), \quad (1)$$

where P^{Oi} for i = 1 to 4 are powers at the outputs of the MMI itself, and P^{In} is the input power. We then evaluate the performance of the proposed HWP in Section 3.2 based on PCE (η in percent) and insertion loss (IL_H in dB). For an input TE_0 mode, we have:

$$\eta = (P_{TM}^{O4}/(P_{TM}^{O4} + P_{TE}^{O4})) \times 100, \quad (2)$$

$$IL_H = -10 \times \log(P_{TM}^{O4}/P_{TE}^{I4}), \quad (3)$$

where P_{TE}^{I4} and P_{TE}^{O4} are the TE_0 mode powers at the input and output of the O4 waveguide, while P_{TM}^{O4} is the TM_0 mode power at the output of the O4 waveguide. Note that in calculating IL using Eq. (3), the splitting loss by the MMI is neglected.

Table 1
Geometrical parameters, in μm, of the designed multifunctional polarization converter.

$d_{1-4\,(2-3)}$	h_{WG}	h_{SL}	h_{ML}	l_{MMI}	l_{taper}	$l_{HWP\ (QWP)}$	$w_{WG\text{-}1\ (WG\text{-}2)}$	w_{MMI}	w_{taper}
6.75 (2.4)	0.39	0.02	0.03	36	8	6.8 (1.48)	0.34 (0.4)	9	2

In Section 3.3, we assess the presented QWP function according to the transmission contrast, TC, (C_T in dB) between the beating TE_0 and TM_0 modes and insertion loss (IL_Q in dB). Since both QWPs are identical and just mirrored with respect to each other, we will just illustrate the results for the O2 waveguide, where C_T and IL_Q are defined as:

$$C_T = 10 \times \log(T_{TM}^{O2}/T_{TE}^{O2}), \tag{4}$$

$$IL_Q = -10 \times \log((P_{TE}^{O2} + P_{TM}^{O2})/P_{TE}^{I2}), \tag{5}$$

where T_{TM}^{O2} and T_{TE}^{O2} are the transmissions of TM_0 and TE_0 modes through the O2 waveguide, P_{TE}^{O2} and P_{TM}^{O2} are the TE_0 and TM_0 mode powers at the output of the O2 waveguide, while P_{TE}^{I2} is the TE_0 mode power at the input of the O2 waveguide. In calculating IL using Eq. (5), the splitting loss by the MMI is also neglected.

3. Numerical results

3.1. MMI performance

Fig. 2(a) shows the performance of the MMI over C to U telecom bands. According to this figure, all outputs have a transmission of ≥ 22% over the wavelength range of 1.53 to 1.62 μm and the insertion loss is < 0.6 dB. Note that this insertion loss is calculated as the ratio of the sum of the output powers of all outputs to the input power. For the wavelength range of 1.62 to 1.675 μm, the O1 and O4 waveguides keep a transmission of 21%, while transmission in the O2 and O3 waveguides reduces from 22% to 18%, which results in an increased insertion loss of < 1.1 dB, which is still acceptable. As the MMI section was optimized for an initial wavelength of 1.55 μm, in Figs. 2(b) and 2(c) we depicted the two dimensional (2D) electric field distributions in the MMI section at that wavelength. Fig. 2(b) shows how a single TE_0 mode is split inside the MMI region and converges to four modes at the end of this area. The distribution of the electric field in the **YZ** plane is shown in Fig. 2(c) from which the taper's width and the distance between the outputs, i.e. w_{taper}, d_{1-4}, and d_{2-3}, are derived in order to lower the insertion loss as much as possible.

3.2. HWP functionality

Fig. 3 shows the performance of the two-section HWP over the telecom wavelength range of 1.53 to 1.675 μm, i.e. C to U bands. Fig. 3 shows the PCE for both the two-section HWP (denoted by η_{2s}) and the conventional one-section HWP (denoted by η_{1s}) to show the superior performance of our design to the conventional one. As shown in Fig. 3, η_{2s} is ≥ 91% over the whole C to U bands with a maximum of 99.95% at λ_0 = 1.563 μm. More importantly, the proposed two-section HWP illustrates a 0.2 dB bandwidth of 125 nm for η_{2s} of ≥ 95%, i.e. ~ 86% of the C to U telecom bands. In contrast, the one-section HWP has a η_{1s} of ≥ 91% for the wavelength range of λ_0 = 1.53 to 1.615 μm, even not covering the whole C and L bands. Moreover, this coupler has a 0.2 dB bandwidth of only 39 nm for η_{1s} of ≥ 95%. The comparison of the performance of the conventional HWP with our proposed two-section HWP shows indeed the latter case outperforms the one-section HWP. The very large PCE over 125 nm of the C to U bands makes our proposed two-section HWP device potentially attractive for mode/polarization (de)multiplexing. As the two-section HWP shows its advantage over the conventional one, we continue with the two-section HWP. According to the right **Y** axis in this figure, IL of our HWP ($IL_{H\text{-}2s}$) varies between 5.4 to 7.9 dB with its minimum at λ_0 = 1.563 μm. At first glance, the IL range might seem a bit high compared to some recent works on plasmonic HWPs, but we should notice that we used a two-section HWP in contrast to earlier reports. Due to the use of two-section HWP, the length of gold metal layer is l_{HWP} = 6.8 μm, which consequently increases the loss by only 2.7 to 4 dB. However, according to the results in Fig. 3 and as demonstrated in [31], from the application perspective of our proposed device, in the trade-off between IL, ultrabroad operation range, and much higher PCE, we prioritized the latter two performance parameters. Finally, the reflection from the HWP back to the MMI is calculated, which is lower than −18.8 dB throughout the whole wavelength range, with its minimum value of −29.5 dB at λ_0 = 1.563 μm.

Fig. 4 shows the performance of the two-section HWP by presenting the 2D electric field distribution through the O4 waveguide at λ_0 = 1.563 μm, where the PCE is 99.95%. Based on Figs. 4(a) and 4(b), the distribution of the electric field components E_y and E_z along the propagation direction of light inside the waveguide illustrates the beating pattern between the two excited modes in the HWP region, indicated as an overlay in these figures (see Fig. 1(c) for the layout of the HWP). As elaborated in [31], we designed our two-section HWP in a way that uses the combination of a QWP and a TQWP, which ultimately converts an input TE_0 mode to an output TM_0 mode with the highest possible PCE. Figs. 4(c) and 4(d) show the intensity profiles of the electric field components E_z and E_x at the waveguide's output port of O4, where the latter is the longitudinal component of the waveguide mode. Both the profiles clearly show the existence of a TM_0 mode at the output.

In order to quantitatively present the polarization state of the propagating light before and after the HWP, we used the polarization ellipse which provides information about both the polarization angle and ellipticity of the light mode. From the

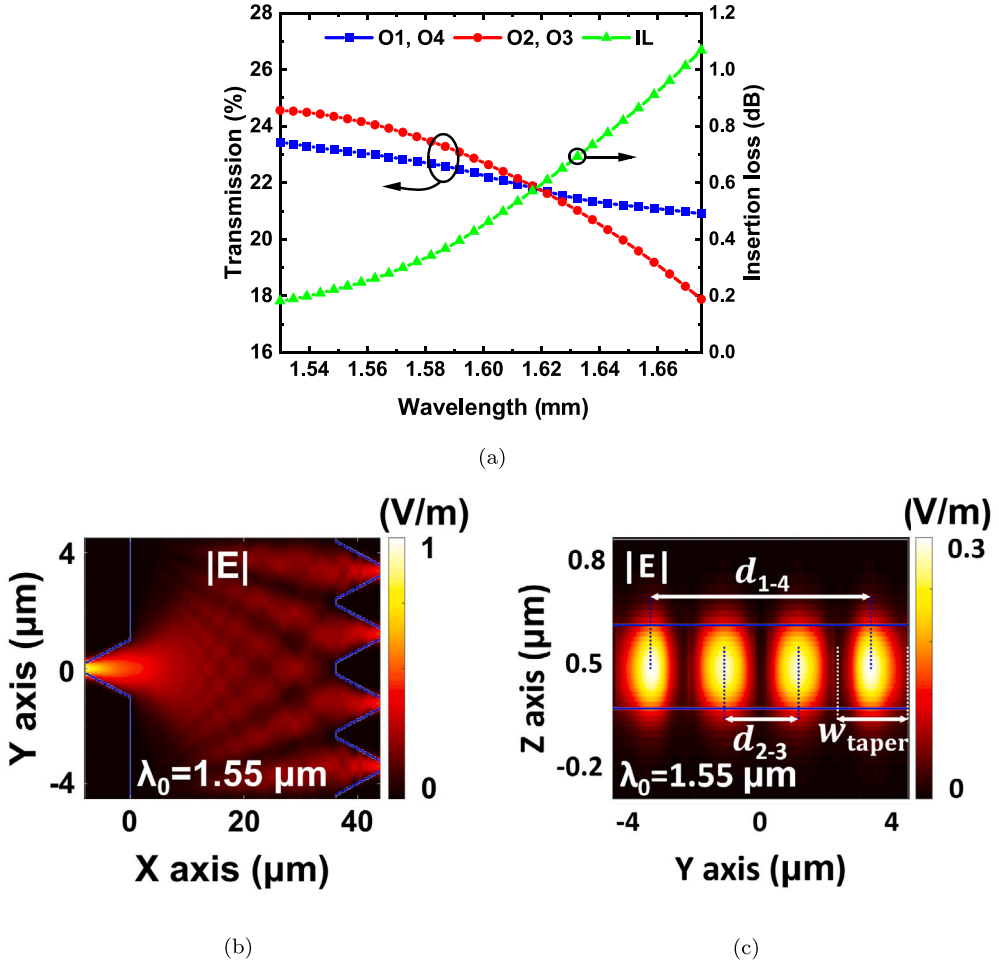

Fig. 2. Performance of the MMI section over the telecom wavelength range of C to U, i.e. λ_0 = 1.53 to 1.675 μm. (a) Transmission of individual output waveguides, O1 to O4, and the insertion loss (IL) of MMI at the left and right **Y** axes, respectively. (b, c) The two dimensional (2D) electric field distribution across the MMI section in the **XY** plane, and at the end of MMI in the **YZ** plane. w_{taper}, d_{1-4}, and d_{2-3} are the width of the taper and distances between the outputs 1–4 and 2–3, respectively.

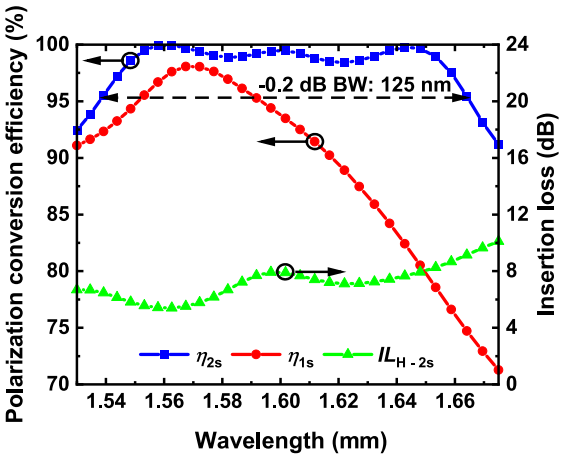

Fig. 3. Performance of the two-section HWP (denoted by 2s) over the telecom wavelength range of C to U, i.e. λ_0 = 1.53 to 1.675 μm. Polarization conversion efficiency and IL (η_{2s} and $IL_{H\text{-}2s}$) at the left and right **Y** axes, respectively. For comparison, the η_{1s} of the one-section HWP is also plotted.

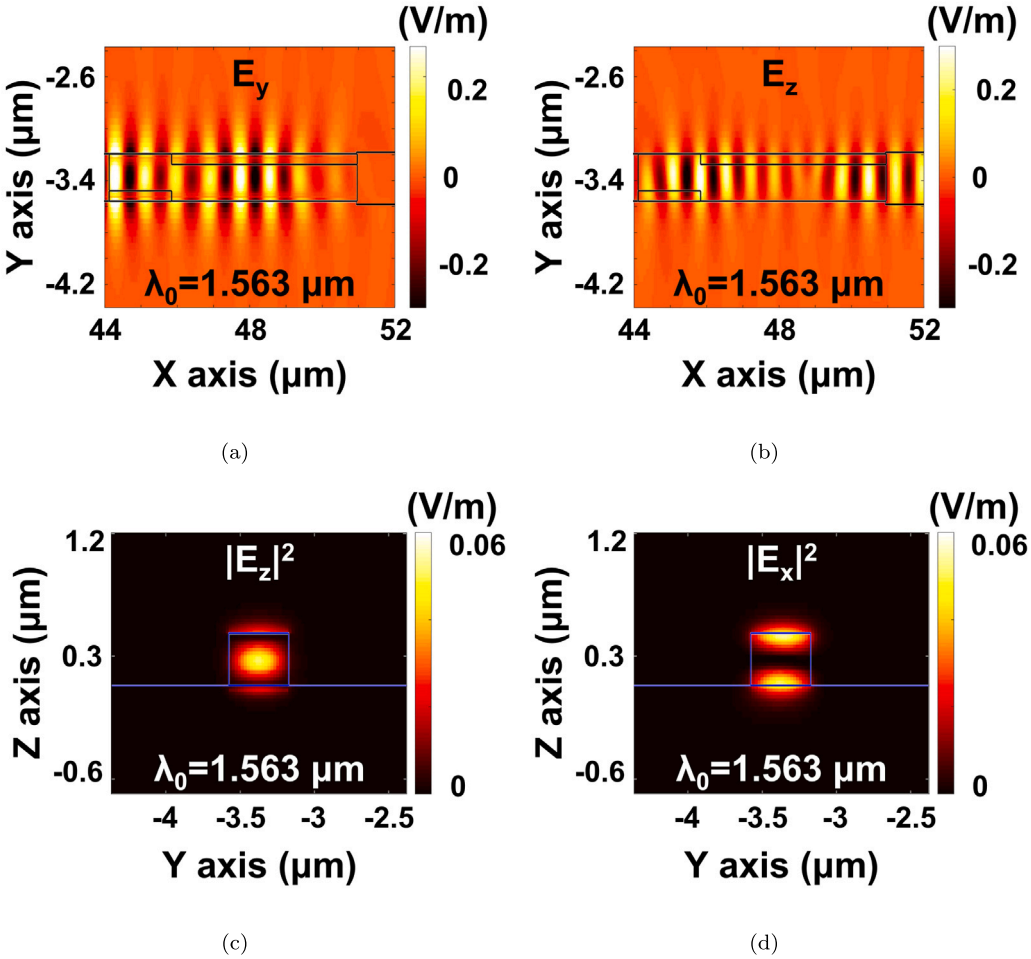

Fig. 4. The 2D electric field distribution in the O4 waveguide for the two-section HWP at λ_0 = 1.563 μm. (a, b) The electric field components E_y and E_z of the light propagating through the waveguide, respectively. (c, d) The intensity profiles of the electric field components E_z and E_x respectively, illustrating the emergence of a TM_0 mode. The layouts of the structures are also shown as an overlay.

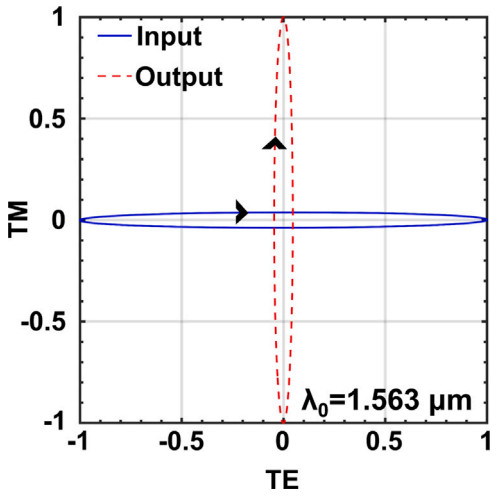

Fig. 5. Illustration of the polarization state of light using the polarization ellipse at λ_0 = 1.563 μm for the HWP.

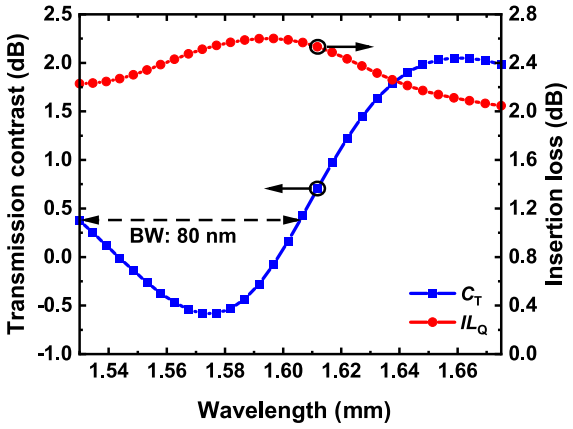

Fig. 6. Performance of QWP over the telecom wavelength range of C to U, i.e. λ_0 = 1.53 to 1.675 μm. Transmission contrast and IL (C_T and IL_Q) at the left and right **Y** axes, respectively.

polarization ellipse of the input TE_0 mode in Fig. 5, we obtained the polarization angle of $\theta = 0.07°$ and the ellipticity angle of $\chi = 2°$ using the following equations [43]:

$$\tan 2\theta = \frac{2E_y E_z \cos\phi}{E_y^2 - E_z^2}, \tag{6}$$

$$\sin 2\chi = \frac{2E_y E_z \sin\phi}{E_y^2 + E_z^2}, \tag{7}$$

where $0 \le \theta \le 180°$, $-45° \le \chi \le 45°$, and ϕ is the phase difference between the electric field components E_y and E_z at a given wavelength. At the output port of O4, the waveguide mode is rotated and the polarization angle reached to $\theta = 89.9°$ and $\chi = 4°$, resulting in the emergence of a TM_0 mode. Based on the results presented in Figs. 4 and 5, one can see the proper functionality of the proposed two-section HWP, while the results in Fig. 3 demonstrates that our two-section HWP outperforms the conventional one-section HWP.

3.3. QWP functionality

The proposed device can also provide QWP functionality as it delivers two quasi-circular polarized beams with opposite spins, by placing them mirrored relative to each other, one on the O2 waveguide and the other on the O3 waveguide. Because of this symmetry, we just show the performance of one of the QWP designs as shown in Fig. 6. In order to have a QWP that properly works, the transmission contrast between the TM_0 and TE_0 modes must be ≈ 0 dB. According to the left **Y** axis of Fig. 6, the transmission contrast of $|C_T| < 0.6$ dB fulfills this criterion over the wavelength range of 1.53 to 1.61 μm, i.e. a bandwidth of 80 nm, which fully covers the C band and 55% of the C to U telecom bands. The right **Y** axis in this figure presents IL of the proposed QWP in which one can see that IL_Q varies between 2 to 2.6 dB across this ultrabroad wavelength range. It is noteworthy mentioning that the reflection is better than −20 dB over the same wavelength range.

The distributions of the electric field magnitude |E| across the O2 and O3 waveguides are plotted in Figs. 7(a) and 7(b) at λ_0 = 1.597 μm, where C_T is 0 dB. As also denoted in these figures, it can be seen that the electric field spins in the plane of the propagation in both channels due to the transverse SAM [28], where the light beam in O2 has a $\sigma-$ spin, while it has a $\sigma+$ spin in O3.

The field distributions in Figs. 7(a) and 7(b) also show that the profile of the propagating beam changes as it enters the second section of the waveguide (WG-2, see Fig. 1(b)) as denoted by a white dashed line. As mentioned in Section 2, we linked the O2 and O3 waveguides with two waveguides with different widths, where the second part with the width of $d_{WG\text{-}2}$ is designed to suppress the birefringence in the waveguide effectively. In this way, we will have quasi-circular polarized light beams in O2 and O3 that carry longitudinal OAM [28,29]. To illustrate this more, we presented the intensity and phase profiles of the longitudinal component of the electric field, i.e. E_x, in Figs. 7(c) to 7(f) for both O2 and O3, respectively. According to Figs. 7(c) and 7(d), there is a point of zero intensity in the intensity profiles of E_x in both outputs. In addition, the phase profiles of E_x in O2 and O3 have a spiral-shaped front as presented in Figs. 7(e) and 7(f). Both these features are characteristics of longitudinal OAM in a photonic waveguide [27–29]. It is worth mentioning that the detailed explanation on SAM and OAM is outside of the scope of this work and interested readers are referred to [44–46] for a detailed description. Overall, one can see that our PC device can provide another degree of freedom by creating two optical beams carrying SAM and OAM with $l = \pm 1$ from only a TE_0 polarized light beam, without changing the propagation direction.

Similar to what is done in Section 3.2, in order to quantitatively illustrate the change in the polarization state of the input light, the polarization ellipse is used, for which the results are presented in Fig. 8. Likewise, we have a TE_0 input light mode which is converted to two quasi-circular polarized beams. Based on the results, the ellipticity and polarization angles of the output fields of the O2 and O3 waveguides are equal to $\chi = 45°$ and $\theta = 45°$.

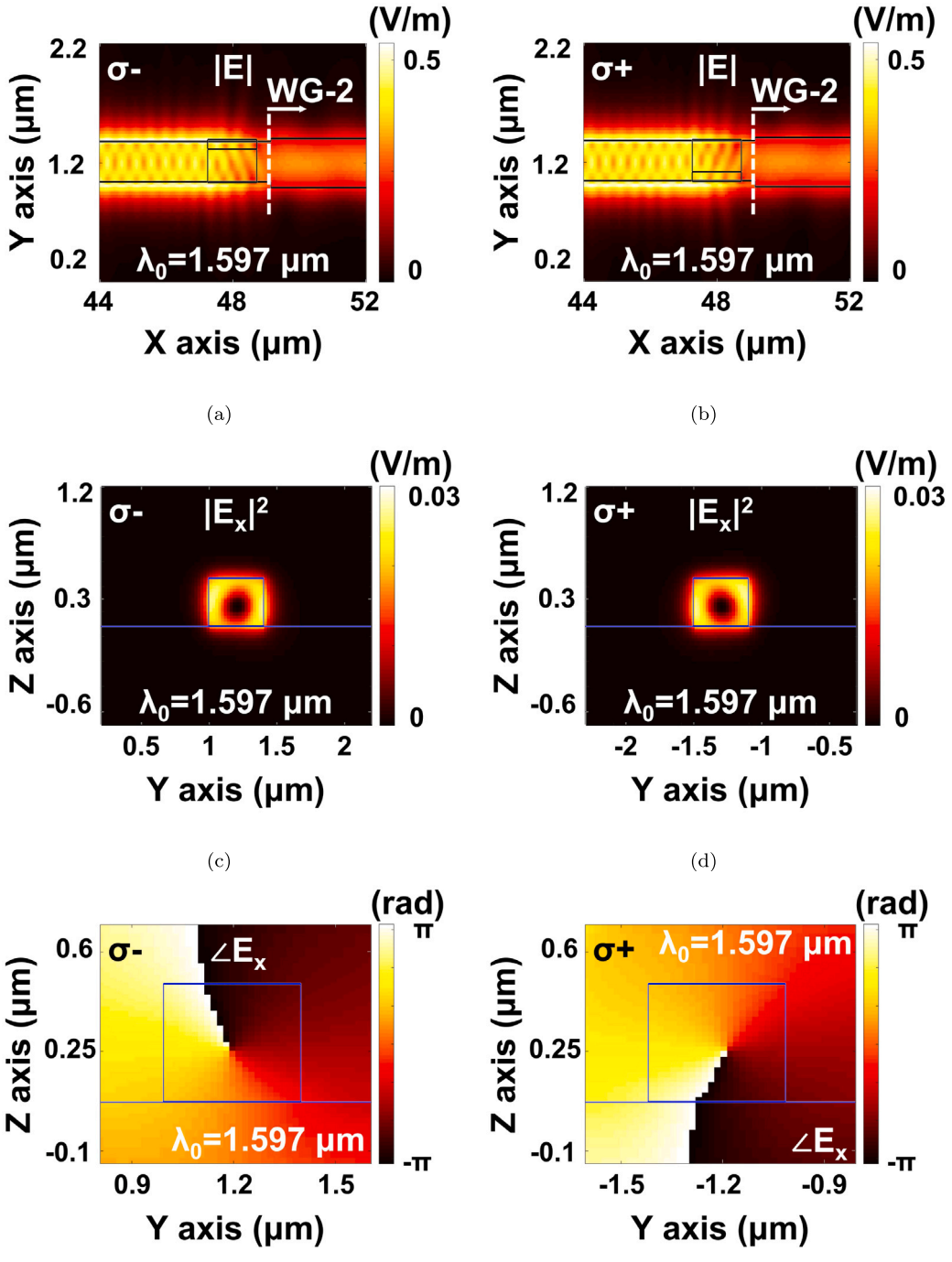

Fig. 7. The 2D electric field distribution in the O2 and O3 waveguides for QWP at λ_0 = 1.597 μm. (a, b) The electric field magnitude |E| of light propagating through the waveguide for two opposite spins of $\sigma-$ and $\sigma+$, respectively. (c, d) The intensity profiles of the electric field component E_x at the waveguide's output ports for $\sigma-$ and $\sigma+$, respectively. (e, f) The phase profiles ($\angle E_x$) of the electric field component E_x at the waveguide's output ports for $\sigma-$ and $\sigma+$, respectively. The layouts of the structures are also shown as an overlay.

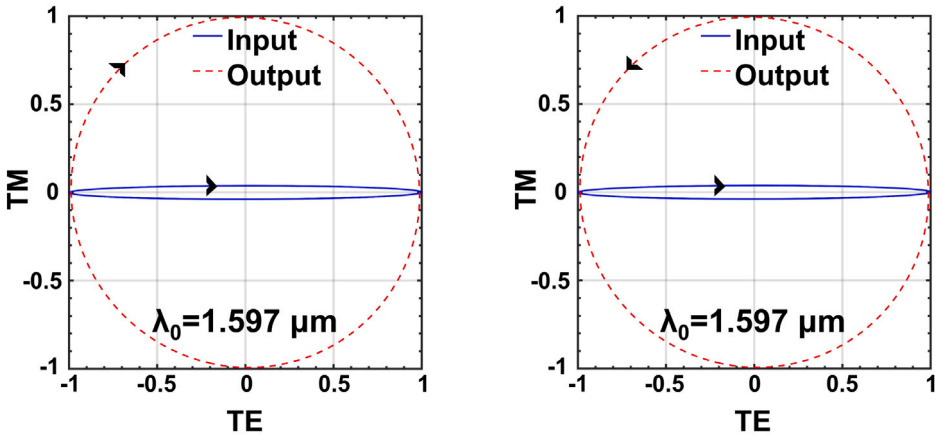

Fig. 8. Illustration of the polarization state of light using the polarization ellipse at λ_0 = 1.597 μm for the QWP. (a, b) $\sigma-$ and $\sigma+$ spins in the O2 and O3 waveguides, respectively.

Table 2
Performance overview of the previously reported half-wave plates and that of our device.

Device	PCE (%)	Bandwidth (nm)	IL (dB)
[16]	90	60	11
[17]	50	150	2.1
[24]	95	70	1.5
[25]	99	35	4.7
This work	≥ 95	125	< 8

4. Discussion

Based on the results in Section 3, we illustrated that our device can offer a HWP functionality. This device converts an input TE_0 mode into a TM_0 mode with an efficiency of ≥ 91% over the entire C to U telecom bands, while it offers a 0.2 dB bandwidth of 125 nm with a PCE of ≥ 95%. Note that a PCE of ≥ 95% corresponds to a PER of larger than 13 dB. In comparison to the recently published works on HWPs [16,17,24,25], our device benefits from very efficient conversion efficiency, very large polarization extinction ratio, and ultra broadband operational window see Table 2). Moreover, due to the application of the two-section technique, our HWP can also offer high tolerance to fabrication errors as demonstrated in [31], while keeping the IL below 8 dB. It is noteworthy mentioning that the IMOS-platform offers semiconductor optical amplifier (SOA)-functionality to compensate the losses.

In addition, our proposed device can efficiently create two quasi-circular polarized light beams with opposite spins. Results showed that this device can maintain QWP functionality over the whole C band and 55% of the C to U telecom bands, while IL remains below 2.6 dB. In contrast, in the recent reports on integrated QWPs [26–29,47], the broadband operation of QWP, and the possibility of having light beams with two opposite spins on the same chip without reversing the propagation direction of a TE_0 or a TM_0 light mode have not been investigated. From the fabrication perspective, if common fabrication errors give rise to birefringence in the O2 and O3 output waveguides, we can suggest the use of phase-change materials, e.g. germanium–antimony–tellurium (GST), to control and minimize the birefringence in the waveguides [48].

The proposed device in this paper supports polarization demultiplexing with a wide applications range from telecom to biosensing. From an input TE_0 mode, our device can create a TM_0 light mode and two quasi-circular polarized light beams. The TE_0 to TM_0 conversion can serve as a polarization degree of freedom for quantum information processing. The generated light beams by QWPs can carry SAM and OAM with $l = \pm 1$, which can be quite useful in quantum information processing by offering the OAM degree of freedom, i.e. encoding signals with opposite topological charges.

5. Conclusion

To conclude, we numerically demonstrated a multifunctional integrated plasmonic–photonic device based on a compact 1 × 4 MMI for polarization demultiplexing in the IMOS platform. This device can offer the HWP and QWP functionalities with high efficiency over the 86.2% and 55% of the C to U telecom bands, i.e. λ_0 = 1.53 to 1.675 μm, respectively. Our device with such characteristics can be a potential building block for controlling the light polarization in PICs, which not only is important for on-chip telecom applications, but also can have advantages for biosensing area. Finally, we expect that the device in this paper can act

as a key photonic component for quantum information processing by offering both polarization and angular momentum degrees of freedom.

Declaration of competing interest

The authors declare that they have no known competing financial interests or personal relationships that could have appeared to influence the work reported in this paper.

Data availability

Data will be made available on request.

Acknowledgments

This work is part of the Gravitation program 'Research Centre for Integrated Nanophotonics', which is financed by the Netherlands Organization for Scientific Research (NWO).

References

[1] J.J. van der Tol, Y. Jiao, L. Shen, A. Millan-Mejia, V. Pogoretskii, J.P. van Engelen, M.K. Smit, Indium phosphide integrated photonics in membranes, IEEE J. Sel. Top. Quantum Electron. 24 (1) (2017) 1–9.
[2] J.J. van der Tol, Y. Jiao, J.P. van Engelen, V. Pogoretskiy, A.A. Kashi, K. Williams, InP membrane on silicon (IMOS) photonics, IEEE J. Quantum Electron. 56 (1) (2019) 1–7.
[3] F.A. Kish, D. Welch, R. Nagarajan, J.L. Pleumeekers, V. Lal, M. Ziari, A. Nilsson, M. Kato, S. Murthy, P. Evans, et al., Current status of large-scale InP photonic integrated circuits, IEEE J. Sel. Top. Quantum Electron. 17 (6) (2011) 1470–1489.
[4] H. Pezeshki, A.J. Wright, E.C. Larkins, Ultra-compact and ultra-broadband hybrid plasmonic-photonic vertical coupler with high coupling efficiency, directivity, and polarisation extinction ratio, IET Optoelectron. 16 (3) (2022) 124–132.
[5] Y. Jiao, J.J.G.M. van der Tol, K. Williams, InP membrane technology for photonics electronics convergence, in: 2020 Opto-Electronics and Communications Conference, OECC, IEEE, 2020, pp. 1–3.
[6] D. Dai, L. Liu, S. Gao, D.-X. Xu, S. He, Polarization management for silicon photonic integrated circuits, Laser Photonics Rev. 7 (3) (2013) 303–328.
[7] W. Bogaerts, D. Taillaert, P. Dumon, D. Van Thourhout, R. Baets, E. Pluk, A polarization-diversity wavelength duplexer circuit in silicon-on-insulator photonic wires, Opt. Express 15 (4) (2007) 1567–1578.
[8] T. Barwicz, M.R. Watts, M.A. Popović, P.T. Rakich, L. Socci, F.X. Kärtner, E.P. Ippen, H.I. Smith, Polarization-transparent microphotonic devices in the strong confinement limit, Nature Photonics 1 (1) (2007) 57–60.
[9] D. Dai, J. Bauters, J.E. Bowers, Passive technologies for future large-scale photonic integrated circuits on silicon: Polarization handling, light non-reciprocity and loss reduction, Light Sci. Appl. 1 (3) (2012) e1–e12.
[10] J. Zhang, M. Yu, G.-Q. Lo, D.-L. Kwong, Silicon-waveguide-based mode evolution polarization rotator, IEEE J. Sel. Top. Quantum Electron. 16 (1) (2009) 53–60.
[11] D. Dai, J.E. Bowers, Novel concept for ultracompact polarization splitter-rotator based on silicon nanowires, Opt. Express 19 (11) (2011) 10940–10949.
[12] A. Barh, B.A. Rahman, R.K. Varshney, B.P. Pal, Design and performance study of a compact SOI polarization rotator at 1.55 μm, J. Lightwave Technol. 31 (23) (2013) 3687–3693.
[13] J. Wang, B. Niu, Z. Sheng, A. Wu, W. Li, X. Wang, S. Zou, M. Qi, F. Gan, Novel ultra-broadband polarization splitter-rotator based on mode-evolution tapers and a mode-sorting asymmetric Y-junction, Opt. Express 22 (11) (2014) 13565–13571.
[14] S. Keyvaninia, H. Boerma, M. Wössner, F. Ganzer, P. Runge, M. Schell, Highly efficient passive InP polarization rotator-splitter, Opt. Express 27 (18) (2019) 25872–25881.
[15] Z. Wang, D. Dai, Ultrasmall Si-nanowire-based polarization rotator, J. Opt. Soc. Amer. B 25 (5) (2008) 747–753.
[16] J. Zhang, S. Zhu, H. Zhang, S. Chen, G.-Q. Lo, D.-L. Kwong, An ultracompact surface plasmon polariton-effect-based polarization rotator, IEEE Photonics Technol. Lett. 23 (21) (2011) 1606–1608.
[17] J.N. Caspers, M.Z. Alam, M. Mojahedi, Compact hybrid plasmonic polarization rotator, Opt. Lett. 37 (22) (2012) 4615–4617.
[18] H. Deng, D.O. Yevick, C. Brooks, P.E. Jessop, Design rules for slanted-angle polarization rotators, J. Lightwave Technol. 23 (1) (2005) 432–445.
[19] C. Brooks, P.E. Jessop, H. Deng, D. Yevick, N.G. Tarr, Passive silicon-on-insulator polarization-rotating waveguides, Opt. Eng. 45 (4) (2006) 044603.
[20] W. Jiang, Fabrication-tolerant polarization splitter and rotator based on slanted silicon waveguides, IEEE Photonics Technol. Lett. 30 (7) (2018) 614–617.
[21] S.-H. Kim, R. Takei, Y. Shoji, T. Mizumoto, Single-trench waveguide TE-TM mode converter, Opt. Express 17 (14) (2009) 11267–11273.
[22] A.V. Velasco, M.L. Calvo, P. Cheben, A. Ortega-Moñux, J.H. Schmid, C.A. Ramos, Í.M. Fernandez, J. Lapointe, M. Vachon, S. Janz, et al., Ultracompact polarization converter with a dual subwavelength trench built in a silicon-on-insulator waveguide, Opt. Lett. 37 (3) (2012) 365–367.
[23] K. Nakayama, Y. Shoji, T. Mizumoto, Single trench SiON waveguide TE-TM mode converter, IEEE Photonics Technol. Lett. 24 (15) (2012) 1310–1312.
[24] L. Gao, Y. Huo, J.S. Harris, Z. Zhou, Ultra-compact and low-loss polarization rotator based on asymmetric hybrid plasmonic waveguide, IEEE Photonics Technol. Lett. 25 (21) (2013) 2081–2084.
[25] M.-A. Komatsu, K. Saitoh, M. Koshiba, Compact polarization rotator based on surface plasmon polariton with low insertion loss, IEEE Photon. J. 4 (3) (2012) 707–714.
[26] L. Gao, Y. Huo, K. Zang, S. Paik, Y. Chen, J.S. Harris, Z. Zhou, On-chip plasmonic waveguide optical waveplate, Sci. Rep. 5 (1) (2015) 1–6.
[27] Y. Liang, F. Zhang, J. Gu, X.G. Huang, S. Liu, Integratable quarter-wave plates enable one-way angular momentum conversion, Sci. Rep. 6 (1) (2016) 1–8.
[28] G. Maltese, Y. Halioua, A. Lemaître, C. Gomez-Carbonell, E. Karimi, P. Banzer, S. Ducci, Towards an integrated AlGaAs waveguide platform for phase and polarisation shaping, J. Opt. 20 (5) (2018) 05LT01–05LT08.
[29] F.C. Ni, Z.T. Xie, X.-D. Hu, C.-Y. Jia, X.G. Huang, Selective angular momentum generator based on a graphene hybrid plasmonic waveguide, J. Lightwave Technol. 37 (21) (2019) 5486–5492.
[30] J. Sui, D. Zhang, H. Zhang, Logical OR operation and magnetic field sensing based on layered topology, J. Phys. D: Appl. Phys. 55 (41) (2022) 415001.
[31] J.J. van der Tol, M. Felicetti, M.K. Smit, Increasing tolerance in passive integrated optical polarization converters, J. Lightwave Technol. 30 (17) (2012) 2884–2889.
[32] Lumerical Inc, FDTD, 2021, https://www.lumerical.com/products/fdtd/.

[33] Z. Guo, L. Zhu, K. Guo, F. Shen, Z. Yin, High-order dielectric metasurfaces for high-efficiency polarization beam splitters and optical vortex generators, Nanoscale Res. Lett. 12 (1) (2017) 1–8.
[34] K. Guo, Q. Zheng, Z. Yin, Z. Guo, Generation of mode-reconfigurable and frequency-adjustable OAM beams using dynamic reflective metasurface, IEEE Access 8 (2020) 75523–75529.
[35] H. Pezeshki, Highly efficient, ultra-compact, and ultra-broadband bidirectional vertical coupler based on spin-directional locking, J. Opt. Soc. Amer. B 39 (10) (2022) 2714–2722.
[36] H. Pezeshki, P. Li, R. Lavrijsen, J.J. van der Tol, B. Koopmans, Optical reading of nanoscale magnetic bits in an integrated photonic platform, IEEE J. Quantum Electron. 59 (3) (2023) 1–8.
[37] H. Pezeshki, P. Li, R. Lavrijsen, M. Heck, E. Bente, J.J. van der Tol, B. Koopmans, Integrated hybrid plasmonic-photonic device for all-optical switching and reading of spintronic memory, Phys. Rev. Appl. 19 (5) (2023) 054036.
[38] F. Flamini, N. Spagnolo, F. Sciarrino, Photonic quantum information processing: A review, Rep. Progr. Phys. 82 (1) (2018) 016001–016032.
[39] X. Wang, Z. Tang, Circular dichroism studies on plasmonic nanostructures, Small 13 (1) (2017) 1601115.
[40] S. Kawata, T. Tani, Optically driven Mie particles in an evanescent field along a channeled waveguide, Opt. Lett. 21 (21) (1996) 1768–1770.
[41] E.D. Palik, Handbook of Optical Constants of Solids, Vol. 3, Academic Press, 1998.
[42] P.B. Johnson, R.-W. Christy, Optical constants of the noble metals, Phys. Rev. B 6 (12) (1972) 4370–4379.
[43] E. Collett, Field Guide to Polarization, SPIE Bellingham, WA, 2005.
[44] A. Aiello, P. Banzer, M. Neugebauer, G. Leuchs, From transverse angular momentum to photonic wheels, Nature Photonics 9 (12) (2015) 789–795.
[45] K.Y. Bliokh, F.J. Rodríguez-Fortuño, F. Nori, A.V. Zayats, Spin–orbit interactions of light, Nature Photonics 9 (12) (2015) 796–808.
[46] K.Y. Bliokh, F. Nori, Transverse and longitudinal angular momenta of light, Phys. Rep. 592 (2015) 1–38.
[47] J. Guo, Y. Liang, X.G. Huang, B. Guo, J. Li, Pure dielectric waveguides enable compact, ultrabroadband wave plates, IEEE Photon. J. 8 (5) (2016) 1–9.
[48] M. Rudé, J. Pello, R.E. Simpson, J. Osmond, G. Roelkens, J.J. van der Tol, V. Pruneri, Optical switching at 1.55 μm in silicon racetrack resonators using phase change materials, Appl. Phys. Lett. 103 (14) (2013) 141119.